Joint Regularization of Phase and Amplitude of InSAR Data: Application to 3D reconstruction

Loïc Denis, Florence Tupin, Jérôme Darbon and Marc Sigelle

Abstract

Interferometric SAR images suffer from a strong noise and their regularization is often a prerequisite for successful use of their information. Independently of the unwrapping problem, interferometric phase denoising is a difficult task due to shadows and discontinuities. In this paper, we propose to jointly filter phase and amplitude data in a Markovian framework. The regularization term is expressed by the minimization of the total variation and may combine different information (phase, amplitude, optical data). First, a fast and approximate optimization algorithm for vectorial data is briefly presented. Then two applications are described. The first one is a direct application of this algorithm for 3D reconstruction in urban areas with Very High Resolution (VHR) images. The second one is an adaptation of this framework to the fusion of SAR and optical data. Results on aerial SAR images are presented.

I. Introduction

The two previous years have seen a new generation of SAR sensors (TerraSAR-X [33], ALOS, CSK [26], RadarSat-2) with increased resolution and smaller revisit time thanks to constellation. Although very popular for their all-weather and all-time capabilities and their polarimetric and interferometric potential, SAR data remain difficult to use and processing tools are still necessary to fully benefit from them. In this paper, we propose a new filtering tool for interferometric SAR data and investigate its application for 3D reconstruction with or without the help of an additional optical image.

Since the seminal work of Geman and Geman [15], Markovian approaches have proved to be very efficient tools in image processing. By introducing contextual relationship, they are able to retrieve a fundamental property of images which is the spatial coherence. These methods have been widely applied in different domains: medical imaging, robotic, remote sensing,... In the remote sensing area, they have proven to be efficient for a very wide range of applications : classification [21] [35] [37] [3]; denoising [36] [45] [20]; 3D reconstruction [43] ; change detection [29]. Theses approaches are based on the minimization of an energy which is composed of

This work was supported by the Centre National d'Études Spatiales under the project R-S06/OT04-010.

L. Denis was with Institut TELECOM, TELECOM ParisTech, CNRS LTCI, Paris, France, and is now with École Supérieure de Chimie Physique Électronique de Lyon and Laboratoire Hubert Curien, CNRS UMR 5516, St-Étienne.

F. Tupin and M. Sigelle are with Institut TELECOM, TELECOM ParisTech, CNRS LTCI, Paris, France.

J. Darbon is with the Department of Mathematics of UCLA, Los Angeles, USA. Research supported by ONR Grant N000140710810 and also partially through NSF DMS-0610079 and ONR N00014-06-1-0345.

two terms: a first term representing the link between the restored field and the observed data ("likelihood term" from a probabilistic view point); and a second regularization term which represents the prior knowledge on the solution. The contextual information is usually introduced in this second term by pairwise interaction between pixels. Depending on the likelihood model and regularization potentials used to define these interactions, the global energy may be non convex and therefore difficult to minimize. This difficulty has led to many works. The first solution used in [15] is the famous Simulated Annealing. Although having good theoretical properties of convergence, this stochastic algorithm is computationally heavy. A much faster deterministic approach, the Iterated Conditional Mode [4], is thus widely used despite the lack of guarantee on the global optimality of the found solution. More recently, new optimization approaches have been developed based on the search of minimum cuts in a well chosen graph [7]. This is for instance the optimization technique used in [21] or [29] for remote sensing applications. The interest for such efficient approaches is very important. Indeed, they make it possible to find global optimum for certain classes of energy [18] [11].

Using such approaches (Markovian modeling and graph-cut optimization), this paper is dedicated to interferometric SAR data regularization. Many papers have already been devoted to the filtering of SAR images ([25] and [40] are detailed reviews of the different filtering approaches which have been proposed). Similarly, there have been many works dedicated to the problem of interferometric phase filtering. This filtering can be done as a preliminary step to phase unwrapping as in [19] [42] or incorporated in the unwrapping step [32] [20]. Here, we are interested in the *joint filtering* of amplitude and interferometric phase, in the case where no unwrapping step is necessary. This situation appears when the elevation range is contained within one fringe. It is the case for aerial data with very small baseline. Our aim is to investigate the interest of the joint use of both amplitude and phase data. It is indeed likely that the edges of one image are also present in the other one. We propose here to define a Markovian framework exploiting this property, and to use graph-cut methods to perform the optimization step.

This paper is divided into 3 parts. In the first section, we recall the principle of a recent fast and approximate algorithm [13] for the optimization of Markov Random Fields (MRF) of vectorial data. Details on computational aspects and comparison with other optimization approaches can be found in [13]. In this work, the applicative potential of this kind of framework is emphasized. The application we are considering is the joint filtering of interferometric phase and amplitude (the amplitude representing here the combination of the two amplitude images). Two situations are described, which constitute the main contributions of this paper. The first one is the joint regularization of phase and amplitude data and their use for 3D building reconstruction. Two likelihood models are discussed and associated results are described in section III. The second application is the adaptation of this framework to the fusion of optical and interferometric data. Methodology and results on real data are presented in section IV.

II. Fast and approximate algorithm for TV minimization of vectorial data

A. Problem statement

The problem of joint amplitude and phase filtering can be seen as an optimization problem involving a vector-valued field as unknown. Indeed, the amplitude and phase of each pixel define a vector with two components

and we are looking for a regularized version of this vector at each pixel such that most edges are co-located (joint prior). The proposed MRF models will be described in sections III-B, III-C and IV-C.

Considering that we are dealing with vectorial data, this section briefly recalls the optimization algorithm that will be used in the two following parts of the paper. A more complete description of the method together with a comparison with other optimization approaches may be found in [13]. The graph construction and optimization steps are described to constitute a self-consistent paper.

B. MRF framework

It is assumed that a vectorial image $\boldsymbol{u}$ is defined on a finite discrete lattice S and takes values in a discrete multi-dimensional integer set[1] $\mathcal{L} = \{1, \ldots, L\}^N$ (where N is the dimension, i.e., the number of channels per pixel). We denote by $\boldsymbol{u}_s$ the vectorial value of the image $\boldsymbol{u}$ at the site $s \in S$.

Given an observed image $\boldsymbol{u}$, a Bayesian analysis using the MAP criterion (Maximum A Posteriori) consists of finding a restored image $\boldsymbol{v}$ that maximizes:

$$P(\boldsymbol{v}|\boldsymbol{u}) \propto P(\boldsymbol{u}|\boldsymbol{v})P(\boldsymbol{v}). \tag{1}$$

It can be shown under the assumption of Markovianity of $\boldsymbol{v}$ (with order-2 cliques) and with some independence assumption on $\boldsymbol{u}$ conditionally to $\boldsymbol{v}$ ($P(\boldsymbol{u}|\boldsymbol{v}) = \Pi_s P(\boldsymbol{u}_s|\boldsymbol{v}_s)$) that the MAP problem is an energy minimization problem:

$$\hat{\boldsymbol{v}}^{(MAP)} = \arg\min_{\boldsymbol{v}} E(\boldsymbol{v}|\boldsymbol{u}) \ , \tag{2}$$

with (denoting by s and t indexes representing neighbouring positions of the MRF):

$$E(\boldsymbol{v}|\boldsymbol{u}) = \sum_s U(\boldsymbol{u}_s|\boldsymbol{v}_s) + \beta \sum_{(s,t)} \psi(\boldsymbol{v}_s, \boldsymbol{v}_t) \ , \tag{3}$$

$U(\boldsymbol{u}_s|\boldsymbol{v}_s) = -\log P(\boldsymbol{u}_s|\boldsymbol{v}_s)$ and ψ is a function modeling the negative logarithm of the prior chosen for the solution. β is a hyper-parameter whose role is to balance the respective weight of data fidelity U and regularization ψ terms. In this paper, the ψ functions considered will be convex functions of the difference $\boldsymbol{v}_s - \boldsymbol{v}_t$, as required to apply the combinatorial optimization algorithm described below.

C. Energy minimization problem

Graph-cut based approaches are very efficient methods for MRF optimization. For a certain class of energies, exact optimization can be computed [12], [18], [47], but the size of the graph to build and store in memory is prohibitive. Approximate solutions can be provided by algorithms proposed in [7], but for vectorial data, the size of the space to be explored rapidly becomes prohibitive. We suggest in this section a fast algorithm which is more suitable when large or vectorial data are considered, which is the case for remote sensing applications.

Minimizing a non-convex energy is a difficult task as the algorithm may fall into a local minimum. Algorithms such as the Iterated Conditional Modes [4] require a "good" initialization and then perform local changes (i.e., per-pixel changes based on optimizing the value of pixels one after another) to reduce the energy. The change

[1]the number of quantization levels L may be different in each channel. To simplify the notations we will consider in the following that they are all equal to L

of a single pixel is called a *single move*. Graph-cut approaches provide a way to explore a combinatorial set of changes involving simultaneously all pixels. Following [7], we denote such changes *large moves*. Instead of allowing each pixel to either keep its previous value or change it to a given one (α-expansion), we suggest that each pixel could either remain unchanged or its value be increased (or decreased) by a fixed step. Such an approach has been firstly described independently in [1], [9], [20], [22], [47] and applied recently with unitary steps in [20]. We however use these large moves in a case of non-convex data term. The trial steps are chosen to perform a scaling sampling of the set of possible pixel values. We express the algorithm in the general case of vectorial data.

We first describe the set of large moves considered, then the associated graph construction and the resulting algorithm.

1) Local minimization: In our iterative algorithm we consider at each step all images that lie within a single move from our current solution $\hat{\boldsymbol{v}}^{(n)}$. We denote the set of those images by $\mathscr{S}_{\mathbf{d}}(\hat{\boldsymbol{v}}^{(n)})$:

$$\mathscr{S}_{\mathbf{d}}(\hat{\boldsymbol{v}}^{(n)}) = \{\boldsymbol{v} \,/\, \forall s \in S, \exists k_s \in \{0,1\}, \boldsymbol{v}_s = \hat{\boldsymbol{v}}_s^{(n)} + k_s \mathbf{d}\} \tag{4}$$

is the set of images whose pixel value $\hat{\boldsymbol{v}}_s$ is either unchanged or increased by step $\mathbf{d}$ (the setting of $\mathbf{d}$ will be explained later). We define the "best" move $\hat{\boldsymbol{v}}^{(n)} \mapsto \hat{\boldsymbol{v}}^{(n+1)}$ as the one that minimizes the restriction of the energy to the set $\mathscr{S}_{\mathbf{d}}(\hat{\boldsymbol{v}}^{(n)})$:

$$\hat{\boldsymbol{v}}^{(n+1)} = \underset{\boldsymbol{v} \in \mathscr{S}_{\mathbf{d}}(\hat{\boldsymbol{v}}^{(n)})}{\arg\min} E(\boldsymbol{v}|\boldsymbol{u}). \tag{5}$$

It is shown in [13] that the *local* problem of finding the (best) vectorial field $\hat{\boldsymbol{v}}^{(n+1)}$ located within a single move can be *exactly* solved by computing a minimum cut on a graph (described in next paragraph) for regularization potentials ψ that are convex and that depend only on the difference $\boldsymbol{v}_s - \boldsymbol{v}_t$.

2) Graph construction: The basic principle of graph-cuts for image processing consists of transforming a minimization problem such as equation 3 (MRF maximum a posteriori estimation) into a minimum cut – maximum flow computation on a graph. The search for the "best" large move, i.e., the minimization of the restricted problem 5, can be efficiently performed with a fast min-cut algorithm on a graph built according to the general method of Kolmogorov and Zabih [23]. At iteration $n+1$ where the step $\mathbf{d}$ is given, our problem corresponds to a binary minimization problem: find the set of optimal binary variables $(k_s)_{s \in S}$ that minimize the MRF energy

$$\underset{(k_s)_{s \in S}}{\arg\min} \sum_s U(\boldsymbol{u}_s|\hat{\boldsymbol{v}}_s^{(n)} + k_s \mathbf{d}) + \beta \sum_{(s,t)} \psi(\hat{\boldsymbol{v}}_s^{(n)} + k_s \mathbf{d}, \hat{\boldsymbol{v}}_t^{(n)} + k_t \mathbf{d}). \tag{6}$$

Following the graph construction of [23], we build a directed graph $\mathcal{G}(\mathcal{V}, \mathcal{E})$ with nonnegative edge weights and two terminal vertices: the source $\mathscr{S}$ and the sink $\mathscr{P}$. The graph structure and the edge weights are chosen such that any cut[2] has a cost[3] corresponding to the energy to minimize.

a) Graph topology: We create a vertice for each site s, all connected respectively to the source and the sink through two edges with capacity $c_{s,1}$ (resp. $c_{s,0}$). Finally, each clique (s,t) gives rise to an edge with capacity $c_{s,t}$ (fig. 1). These capacities are decomposed into two components defined in the following paragraphs (i.e., $c_{s,\cdot} = c'_{s,\cdot} + c''_{s,\cdot}$).

[2]a cut is a partition of the vertices into two disjoint sets $\mathcal{S}$ and $\mathcal{P}$ such that $\mathscr{S} \in \mathcal{S}$ and $\mathscr{P} \in \mathcal{P}$

[3]the cost of a cut is defined as the sum of the capacities of edges going from partition $\mathcal{S}$ to $\mathcal{P}$

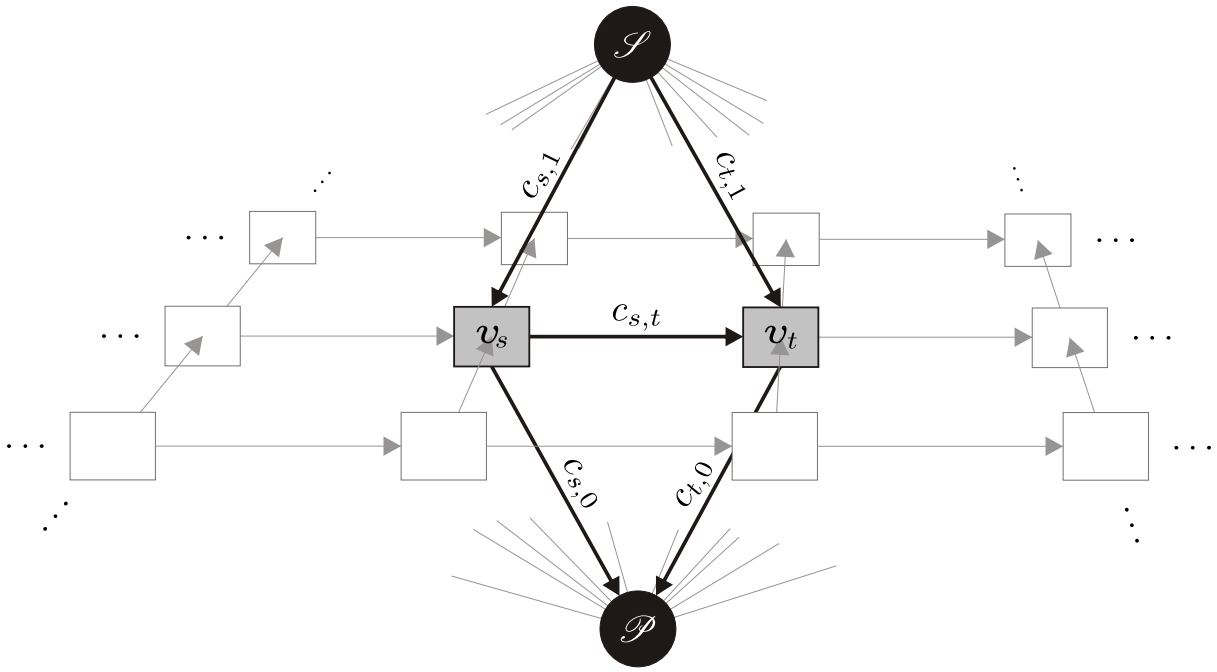

Fig. 1. Graph construction for local minimization: the graph has one layer of nodes (one per pixel) and two terminals (the source $\mathcal{S}$ and the sink $\mathcal{P}$).

b) Representing the log-likelihood term: The first term in equation (6) is represented by the weights:

$$\begin{cases} c'_{s,1} = \max(0, U(\boldsymbol{u}_s|\hat{\boldsymbol{v}}_s^{(n)} + \mathbf{d})) - U(\boldsymbol{u}_s|\hat{\boldsymbol{v}}_s^{(n)})) \\ c'_{s,0} = \max(0, U(\boldsymbol{u}_s|\hat{\boldsymbol{v}}_s^{(n)}) - U(\boldsymbol{u}_s|\hat{\boldsymbol{v}}_s^{(n)} + \mathbf{d}))). \end{cases} \tag{7}$$

c) Representing the log-prior term: To take into account the second term in equation (6), we add the following weights:

$$\begin{cases} c''_{s,1} &= \beta \cdot \max\left(0, \psi(\hat{\boldsymbol{v}}_s^{(n)} + \mathbf{d}, \hat{\boldsymbol{v}}_t^{(n)}) - \psi(\hat{\boldsymbol{v}}_s^{(n)}, \hat{\boldsymbol{v}}_t^{(n)})\right) \\ c''_{s,0} &= \beta \cdot \max\left(0, \psi(\hat{\boldsymbol{v}}_s^{(n)}, \hat{\boldsymbol{v}}_t^{(n)}) - \psi(\hat{\boldsymbol{v}}_s^{(n)} + \mathbf{d}, \hat{\boldsymbol{v}}_t^{(n)})\right) \\ c''_{t,1} &= \beta \cdot \max(0, \psi(\hat{\boldsymbol{v}}_s^{(n)} + \mathbf{d}, \hat{\boldsymbol{v}}_t^{(n)} + \mathbf{d}) \\ & \quad -\psi(\hat{\boldsymbol{v}}_s^{(n)} + \mathbf{d}, \hat{\boldsymbol{v}}_t^{(n)})) \\ c''_{t,0} &= \beta \cdot \max(0, \psi(\hat{\boldsymbol{v}}_s^{(n)} + \mathbf{d}, \hat{\boldsymbol{v}}_t^{(n)}) \\ & \quad -\psi(\hat{\boldsymbol{v}}_s^{(n)} + \mathbf{d}, \hat{\boldsymbol{v}}_t^{(n)} + \mathbf{d})) \\ c''_{s,t} &= \beta \cdot (\psi(\hat{\boldsymbol{v}}_s^{(n)}, \hat{\boldsymbol{v}}_t^{(n)} + \mathbf{d}) + \psi(\hat{\boldsymbol{v}}_s^{(n)} + \mathbf{d}, \hat{\boldsymbol{v}}_t^{(n)}) \\ & \quad -\psi(\hat{\boldsymbol{v}}_s^{(n)}, \hat{\boldsymbol{v}}_t^{(n)}) - \psi(\hat{\boldsymbol{v}}_s^{(n)} + \mathbf{d}, \hat{\boldsymbol{v}}_t^{(n)} + \mathbf{d})) \end{cases} \tag{8}$$

d) Minimum cut computation: Several algorithms have been proposed to compute the minimum flow on a graph. We used an algorithm[4] by Kolmogorov [6] dedicated to the specific structure of graphs arising from computer vision problems. This algorithm typically requires about 100ms to compute a cut on a graph with 256×256 nodes. The actual running time depends on the amount of regularization and increases with the value of hyperparameter β of equation 3. The complexity issues of min-cut computation are discussed in [6]; the complexity of the vectorial data regularization technique is described in [13].

[4]The code is freely available at http://www.adastral.ucl.ac.uk/~vladkolm/software.html.

3) Approximate global minimization: The minimum cut computation on the graph built according to the previous paragraph only solves the sub-problem of finding the best move among the set $\mathscr{S}_{\mathbf{d}}(\hat{\boldsymbol{v}}^{(n)})$. We now consider solving a sequence of min-cut problems to approximatively solve our initial multi-valued minimization problem (i.e., MRF maximum a posteriori estimation). Our approximate minimization is based on a finite number of exact binary optimizations.

To accelerate the exploration, a standard way is to use different scalings of the step $\mathbf{d}$. In one dimension, a scaling search is performed by looking for the best move with steps $d_i^+ = L/2^i$ and $d_i^- = -L/2^i$ for i from 1 to the desired precision (i.e., quantization level), starting from a constant image with value $\frac{L}{2}$. In N dimensions, there are $3^N - 1$ vectorial steps $\mathbf{d}_i$ to consider for a given step size d_i:

$$\mathbf{d}_i \in \mathscr{S}(d_i) \stackrel{\text{def}}{=} \{0, -d_i, +d_i\}^N / \{0, \ldots, 0\}. \tag{9}$$

The regularization algorithm for vectorial data initially proposed in [13] is summarized here:

1: **for all** $s \in S$ **do**
2: $\quad \hat{\mathbf{u}}_s^{(0)} \leftarrow \{L/2, \ldots, L/2\}$
3: **end for**
4: $n \leftarrow 0$
5: **for** $i = 1$ to $precision$ **do**
6: $\quad d_i \leftarrow L/2^i$
7: $\quad$ **for all** $\mathbf{d}_i \in \mathscr{S}(d_i)$ **do**
8: $\quad\quad \hat{\boldsymbol{v}}^{(n+1)} \leftarrow \arg\min_{\boldsymbol{v} \in \mathscr{S}_{\mathbf{d}}(\hat{\boldsymbol{v}}^{(n)})} E(\boldsymbol{v}|\boldsymbol{u})$
9: $\quad\quad n \leftarrow n + 1$
10: $\quad$ **end for**
11: **end for**

Line 8 represents the exact binary energy minimization obtained by computing a minimum cut on a graph built according to section II-C2. The performance of the algorithm (speed, complexity, quality of the optimum) is further studied in [13].

III. Application to 3D reconstruction with InSAR data

In this section, we present an application of the discrete optimization algorithm just described to the joint filtering of interferometric phase and amplitude data for 3D reconstruction purposes [14]. We consider high resolution interferometric data. In case of a small baseline, for instance single-pass aerial data where the two antenna are fixed on the plane, the elevation range is contained within one fringe. The scene may then contain sharp transitions that must be well preserved (i.e., well modeled) in the reconstruction algorithm. We focus in this paper on such non-wrapped phase data. The general problem of phase denoising and unwrapping is much more complex, see paper [20] for a graph-cut based technique that addresses the unwrapping issue.

We consider in the following two MRF models: an approximate likelihood model with separability and partial convexity properties useful for efficient minimization, and an exact likelihood model leading to a more difficult energy minimization problem. The models are applied on real data in paragraph III-D, showing strong noise reduction while preserving edges.

A. Problem statement

Let us denote by $\boldsymbol{z}^{(1)}$ and $\boldsymbol{z}^{(2)}$ the two single look complex (SLC) images in interferometric configuration. From these SLC images, one can derive a 2-looks amplitude image $\boldsymbol{e}$ defined by: $\forall s,\ \boldsymbol{e}_s = \sqrt{\frac{1}{2}|\boldsymbol{z}_s^{(1)}|^2 + \frac{1}{2}|\boldsymbol{z}_s^{(2)}|^2}$. By averaging over a M-samples window centered on site s (sample number i will be denoted $\mathcal{V}_s(i)$ in the following), the interferometric phase, the coherence, and the multi-look intensities can be estimated [27], [41]:

Interferometric phase:	$\boldsymbol{\varphi}$,	$\forall s,\ \boldsymbol{\varphi}_s = \arg\Big[\frac{1}{M}\sum_{i=1}^{M} \boldsymbol{z}^{(1)}_{\mathcal{V}_s(i)} \cdot \mathrm{conj}\Big(\boldsymbol{z}^{(2)}_{\mathcal{V}_s(i)}\Big)\Big]$
Multi-look intensities:	$\boldsymbol{I}^{(1)}$,	$\forall s,\ \boldsymbol{I}^{(1)}_s = \frac{1}{M}\sum_{i=1}^{M}\big\lvert\boldsymbol{z}^{(1)}_{\mathcal{V}_s(i)}\big\rvert^2$
	$\boldsymbol{I}^{(12)}$,	$\forall s,\ \boldsymbol{I}^{(12)}_s = \frac{1}{M}\Big\lvert\sum_{i=1}^{M} \boldsymbol{z}^{(1)}_{\mathcal{V}_s(i)} \cdot \mathrm{conj}\Big(\boldsymbol{z}^{(2)}_{\mathcal{V}_s(i)}\Big)\Big\rvert$
	$\boldsymbol{I}^{(2)}$,	$\forall s,\ \boldsymbol{I}^{(2)}_s = \frac{1}{M}\sum_{i=1}^{M}\big\lvert\boldsymbol{z}^{(2)}_{\mathcal{V}_s(i)}\big\rvert^2$
Coherence:	$\boldsymbol{\rho}$,	$\forall s,\ \boldsymbol{\rho}_s = \frac{\boldsymbol{I}^{(12)}_s}{\sqrt{\boldsymbol{I}^{(1)}_s}\sqrt{\boldsymbol{I}^{(2)}_s}}$.

The problem of 3D reconstruction from interferometric SAR data can be viewed as a regularization problem of the random field $\boldsymbol{\varphi}$. In urban areas, most height discontinuities (i.e., interferometric phase discontinuities) are also accompanied by amplitude discontinuities in SAR images and conversely. The amplitude data can therefore provide useful information to preserve phase differences corresponding to actual height differences while sufficiently smoothing noise in homogeneous areas. We propose to perform joint regularization of phase and amplitude to combine both information sources. The co-location of edges in each restored image is favored by a non-separable regularization potential that penalizes only the largest of the regularized amplitude and phase gradients. Depending on the noisy input-data considered, two options are possible: (a) the 2-looks amplitude $\boldsymbol{e}$ and the $M-$looks interferometric phase $\boldsymbol{\varphi}$ can be jointly regularized, or, (b) the M-look intensities $\boldsymbol{I}^{(1)}$, $\boldsymbol{I}^{(12)}$, and $\boldsymbol{I}^{(2)}$, can be regularized with the corresponding M-look interferometric phase $\boldsymbol{\varphi}$. The first option uses an amplitude image $\boldsymbol{e}$ with better resolution than the $M-$looks phase image $\boldsymbol{\varphi}$. As the prior enforces co-located edges in the regularized amplitude and phase images, one can therefore hope that regularized phase will benefit from the resolution of the input amplitude image $\boldsymbol{e}$. Due to the difference in the number of looks of $\boldsymbol{e}$ and $\boldsymbol{\varphi}$, we use separate likelihood models for each. The corresponding likelihood model is described in paragraph III-B. With option (b) it is possible to use a more precise joint-likelihood model that correctly accounts for the $2\pi-$periodicity of the phase. We present this model in paragraph III-C.

B. MRF model with approximate and separable likelihood

1) Log-likelihood of the amplitude: Under the classical model of Goodman [16], the amplitude $\boldsymbol{e}_s$ of a pixel s follows a Nakagami distribution depending on the square root of the reflectivity $\boldsymbol{a}_s$ and on the number of looks. For a two looks amplitude image, the negative log-likelihood is given by:

$$U(\boldsymbol{e}_s|\boldsymbol{a}_s) = 2\frac{\boldsymbol{e}_s^2}{\boldsymbol{a}_s^2} + 4\log \boldsymbol{a}_s. \tag{10}$$

2) Log-likelihood of the phase: The $M-$looks interferometric phase $\boldsymbol{\varphi}_s$ distribution can be approximated by a Gaussian distribution around the "true" phase ϕ_s, leading to a quadratic negative log-likelihood:

$$U(\boldsymbol{\varphi}_s|\boldsymbol{\phi}_s) = \frac{(\boldsymbol{\varphi}_s - \boldsymbol{\phi}_s)^2}{\hat{\boldsymbol{\sigma}}^2_{\phi_s}}, \tag{11}$$

where the standard deviation $\hat{\boldsymbol{\sigma}}_{\phi_s}$ at site s is set at the Cramer-Rao bound $\hat{\boldsymbol{\sigma}}^2_{\phi_s} = \frac{1-\boldsymbol{\rho}_s^2}{2M\boldsymbol{\rho}_s^2}$. This approximation is acceptable for M at least equal to 6. In low coherence areas (shadows or smooth surfaces), this Gaussian

approximation is less relevant and a uniform distribution model is preferred: $p(\boldsymbol{\varphi}_s|\boldsymbol{\phi}_s) = \frac{1}{2\pi}$. Shadows are therefore detected prior to the regularization, and the likelihood model is set depending whether a pixel is inside or outside the shadow regions.

3) Regularization potential: The minimization of total variation (TV) is a very popular model [8], [10], [28], [30], [31] since the seminal work of [34]. It corresponds to a regularization potential ψ defined as the sum of the absolute difference of neighboring pixels. It has a behavior which preserves discontinuities (i.e., edges) in the regularized signal, while being convex. In the case of urban areas, many sharp discontinuities exist either in the amplitude image or in the interferometric one, so this model is well adapted.

The proposed method aims at preserving *simultaneously* phase and amplitude discontinuities. The phase and amplitude information are hopefully linked since they reflect the same scene. Amplitude discontinuities thus usually have the same location as phase discontinuities and conversely. We propose in this paper to perform the joint regularization of phase and amplitude. To combine the discontinuities a disjunctive $\max$ operator is chosen. The joint prior model is defined by:

$$\psi(\boldsymbol{a}_s - \boldsymbol{a}_t, \boldsymbol{\phi}_s - \boldsymbol{\phi}_t) = \max(|\boldsymbol{a}_s - \boldsymbol{a}_t|, \gamma|\boldsymbol{\phi}_s - \boldsymbol{\phi}_t|), \tag{12}$$

with γ a parameter that can be set to 1, and otherwise accounts for the relative importance given to the discontinuities of the phase ($\gamma > 1$) or of the amplitude ($\gamma < 1$). As requested by the minimization algorithm, this regularization potential is convex.

4) Energy minimization problem: The global joint energy term is then defined as:

$$\begin{aligned} E(\boldsymbol{a}, \boldsymbol{\phi}|\boldsymbol{e}, \boldsymbol{\varphi}) = & \frac{1}{\beta_a} \sum_s M[\frac{\boldsymbol{e}_s^2}{\boldsymbol{a}_s^2} + 2\log \boldsymbol{a}_s] \\ & + \frac{\gamma}{\beta_\phi} \sum_s \frac{(\boldsymbol{\varphi}_s - \boldsymbol{\phi}_s)^2}{\hat{\boldsymbol{\sigma}}_{\phi_s}^2} + \sum_{(s,t)} \max(|\boldsymbol{a}_s - \boldsymbol{a}_t|, \gamma|\boldsymbol{\phi}_s - \boldsymbol{\phi}_t|). \end{aligned} \tag{13}$$

β_a and β_ϕ are some weightings of the likelihood terms introduced in order to balance the data fidelity and regularization terms.

5) Processing of shadow areas: Due to the specific properties of shadow areas (random phase implying constant negative log-likelihood term), they are separately detected and an adapted regularization term is defined. The regularized fields $\boldsymbol{a}$ and $\boldsymbol{\phi}$ at sites s located inside the detected shadow areas are governed only by the regularization term. We use the same specific prior as in [13] inside the shadows to force the regularization heights to ground level.

C. MRF model with exact joint-likelihood

1) Exact log-likelihood: The joint negative log-likelihood of the $M-$looks intensity and interferometric phase at a given pixel s is parameterized by the "true" amplitude $\boldsymbol{a}_s$, phase $\boldsymbol{\phi}_s$ and coherence $\boldsymbol{\zeta}_s$ as follows [27], [41]:

$$\begin{aligned} U(\boldsymbol{I}_s^{(1)}, \boldsymbol{I}_s^{(12)}, \boldsymbol{I}_s^{(2)}, \boldsymbol{\varphi}_s|\boldsymbol{a}_s, \boldsymbol{\phi}_s, \boldsymbol{\zeta}_s) = & \, 4\log \boldsymbol{a}_s + \\ & \frac{\boldsymbol{I}_s^{(1)} + \boldsymbol{I}_s^{(2)} - 2 \cdot \boldsymbol{I}_s^{(12)} \cdot \boldsymbol{\zeta}_s \cdot \cos(\boldsymbol{\phi}_s - \boldsymbol{\varphi}_s)}{\boldsymbol{a}_s^2(1 - \boldsymbol{\zeta}_s^2)}. \end{aligned} \tag{14}$$

We used in the following the coherence estimate $\boldsymbol{\rho}_s$ instead of the "true" coherence $\boldsymbol{\zeta}_s$. The potential U then depends only on the two unknowns $\boldsymbol{a}_s$ and $\boldsymbol{\phi}_s$.

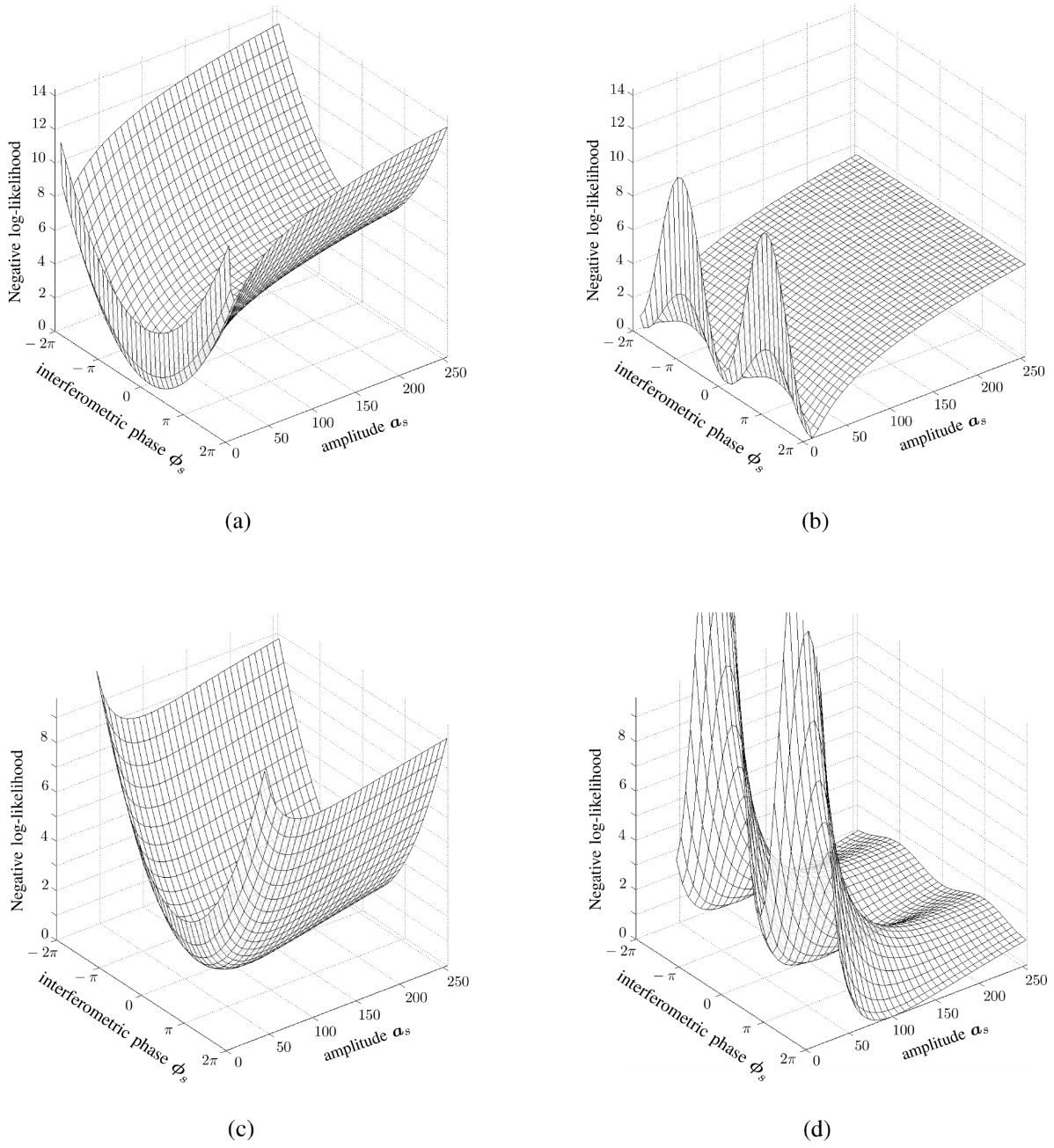

Fig. 2. Negative log-likelihood as a function of the unknown regularized values of the amplitude $\boldsymbol{a}_s$ and interferometric phase $\boldsymbol{\phi}_s$, for a given noisy amplitude (first row: $\boldsymbol{e}_s^2 = \boldsymbol{I}_s^{(1)} = \boldsymbol{I}_s^{(12)} = \boldsymbol{I}_s^{(2)} = 10^2$, second row: $\boldsymbol{e}_s^2 = \boldsymbol{I}_s^{(1)} = \boldsymbol{I}_s^{(12)} = \boldsymbol{I}_s^{(2)} = 10^4$) and a given noisy interferometric phase $\boldsymbol{\varphi}_s = 0$. (a) and (c), separable and approximate model described in paragraph III-B, equations (10) and (11). (b) and (d), exact joint model given in paragraph III-C, equation (14). The model illustrated in subfigures (a) and (c) is separable: it is the sum of a quadratic term and the non-convex negative log-likelihood of the amplitude. The model shown in subfigures (b) and (d) is not separable and is neither convex with respect to the phase, nor with the amplitude. For a given amplitude, the exact model in (b) and (d) is $2\pi-$periodic.

2) Regularization potential: We use the same kind of regularization model as in paragraph III-B3 to preserve the edges and encourage their co-location in the restored amplitude and phase images. Two hyper-parameters β_a and β_ϕ are introduced to balance the amount of smoothing in the regularized field:

$$\psi(\boldsymbol{a}_s - \boldsymbol{a}_t, \boldsymbol{\phi}_s - \boldsymbol{\phi}_t) = \max(\beta_a|\boldsymbol{a}_s - \boldsymbol{a}_t|, \beta_\phi|\boldsymbol{\phi}_s - \boldsymbol{\phi}_t|). \tag{15}$$

3) Energy minimization problem: The global joint energy term is then defined as:

$$\begin{aligned} E(\boldsymbol{I}^{(1)}, \boldsymbol{I}^{(12)}, \boldsymbol{I}^{(2)}, \boldsymbol{\varphi}|\boldsymbol{a}, \boldsymbol{\phi}) = \\ \sum_s \left[\frac{\boldsymbol{I}_s^{(1)} + \boldsymbol{I}_s^{(2)} - 2 \cdot \boldsymbol{I}_s^{(12)} \cdot \boldsymbol{\zeta}_s \cdot \cos(\boldsymbol{\phi}_s - \boldsymbol{\varphi}_s)}{\boldsymbol{a}_s^2(1 - \boldsymbol{\zeta}_s^2)} + 4 \log \boldsymbol{a}_s \right] \\ + \sum_{(s,t)} \max(\beta_a|\boldsymbol{a}_s - \boldsymbol{a}_t|, \beta_\phi|\boldsymbol{\phi}_s - \boldsymbol{\phi}_t|). \end{aligned} \tag{16}$$

This energy is more difficult to minimize than the energy of the separable likelihood model defined in equation 13 due to the non-convexity with respect to both $\boldsymbol{a}$ and $\boldsymbol{\phi}$ and non-separability of the negative log-likelihood. Figure 2 illustrates the two negative log-likelihood models considered. Sub-figures 2(a) (respectively 2(b)) correspond to the separable approximate model (resp. exact joint model) in the case of a noisy amplitude of low level ($\boldsymbol{a}_s$ is in the range $[0,\, 25\boldsymbol{e}_s]$). The non-convexity with respect to the amplitude is clearly visible in both cases (a) and (b): as the regularized amplitude increases, the negative log-likelihood U increases in a slower than linear regime ($U(\boldsymbol{a}_s) \approx 4 \log \boldsymbol{a}_s$ for $\boldsymbol{a}_s$ large with respect to $\boldsymbol{e}_s$ and $\sqrt{\boldsymbol{I}_s}$). For a given regularized amplitude $\boldsymbol{a}_s$, U is quadratic with respect to the regularized phase $\boldsymbol{\phi}_s$ in the approximate case (a), and periodic in the exact model (b). To illustrate the $2\pi-$ periodicity, we displayed U for phase values $\boldsymbol{\phi}_s$ in the $[-2\pi,\, 2\pi]$ interval, i.e. on two periods of the model. The sub-figures (c) and (d) display U in the case of a larger noisy amplitude level ($\boldsymbol{a}_s$ is in the range $[0,\, 2.5\boldsymbol{e}_s]$) for the approximate and exact model respectively.

As the considered data does not require phase unwrapping, we forced the regularized phase $\boldsymbol{\phi}_s$ to be in the $[0,\, 2\pi]$ interval by setting infinite cost to U for $\boldsymbol{\phi}_s$ values outside this interval in the exact likelihood model. To improve the quality of the solution of minimization problem (16), we did two passes of the minimization algorithm: we first decreased the step sizes d from L to 1 and then re-started with steps of size L to 1.

D. Results

The proposed joint regularization model and the fast and approximate regularization algorithm have been applied to two HR RAMSES interferometric images. The sensor parameters are the following: frequency 9.5 GHz(X-band), incidence angle 40°, resolution less than one meter.

The method has been tested on different test areas. One area corresponds to the Bayard quarter, near Dunkerque in the North of France, whereas, the other one corresponds to Toulouse in the South of France.

1) Hyper-parameter setting: The hyper-parameters β_a and β_ϕ of equations 13 and 16 are automatically set using the L-curve method [17]. This curve is the graphical representation of the regularization energy term with respect to the likelihood energy term. The corner of the curve corresponds to a good trade-off between under-regularization (steep part of the curve, where the regularization term can be largely improved with minor likelihood modification) and over-regularization (slowly varying part of the curve, where the regularization

term can no longer be improved, whatever the likelihood price). This method is illustrated in the case of the regularization of SAR amplitude in [13].

2) Joint regularization with approximate likelihood (MRF model of paragraph III-B): The results are presented in figure 4 for the regularized phase and amplitude and in figure 3 for a 3D view.

Fig. 3. 3D view of the amplitude superimposed on the elevation derived from the regularized phase.

The results are very close to the ones obtained in [39] with a very different approach. Note that a weaker hypothesis is made here, since in [39] an assumption of planar surface is done for each region on the optical image. However, a precise comparison is difficult due to the sensor parameters. Indeed, the baseline is 0.7m leading to an ambiguity altitude of 180m and an altimetric precision between 2 and 3 meters. The accuracy of the height retrieval for the large buildings is satisfying (a standard deviation of 2.5 m has been computed) compared to the given altimetric precision.

3) Joint regularization with exact likelihood (MRF model of paragraph III-C): An InSAR image of Toulouse has been processed using the approximate and the exact likelihood models described in paragraphs III-B and

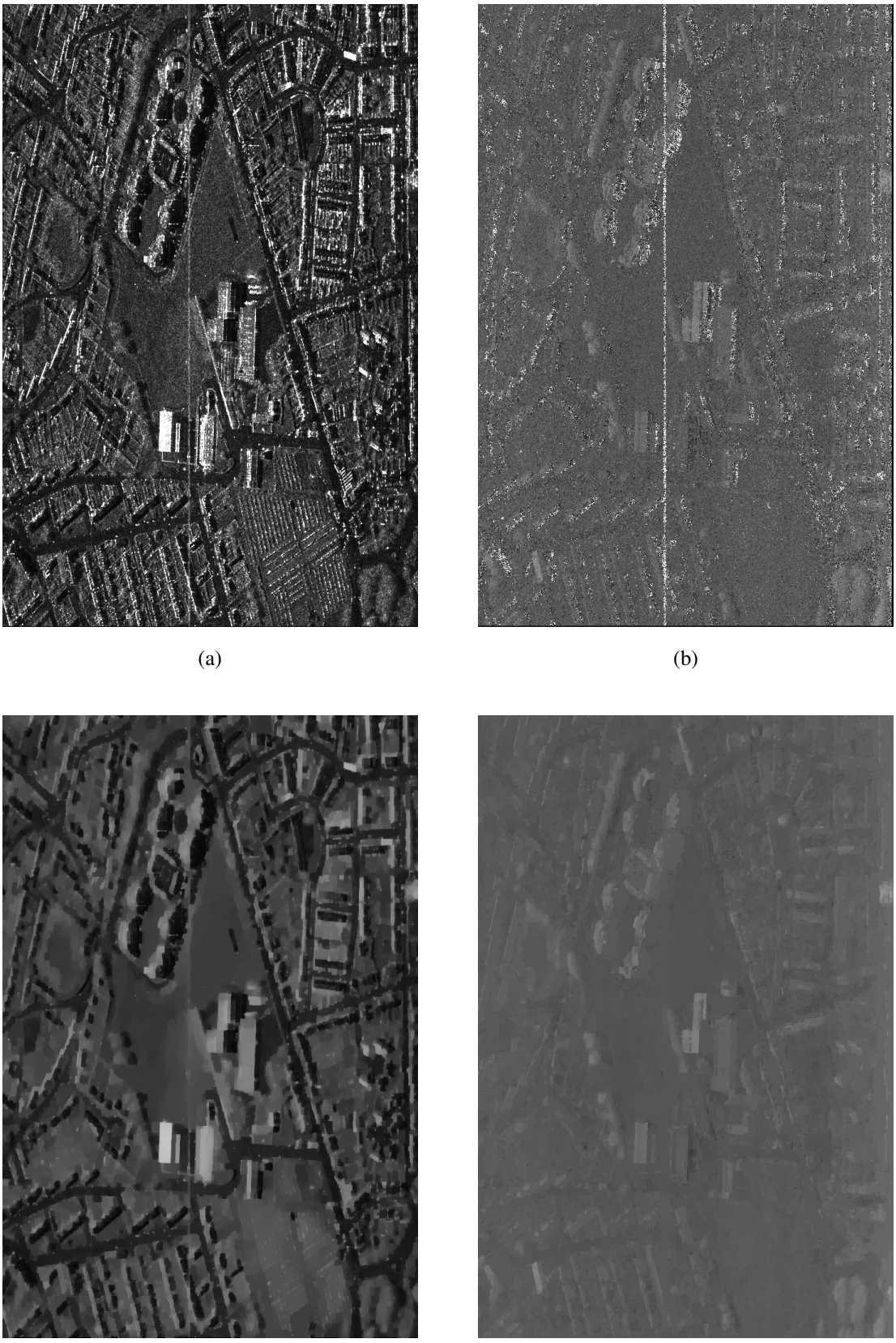

Fig. 4. Original SAR image (on the left amplitude and phase on the right) ©DGA/CNES and their joint regularization (below).

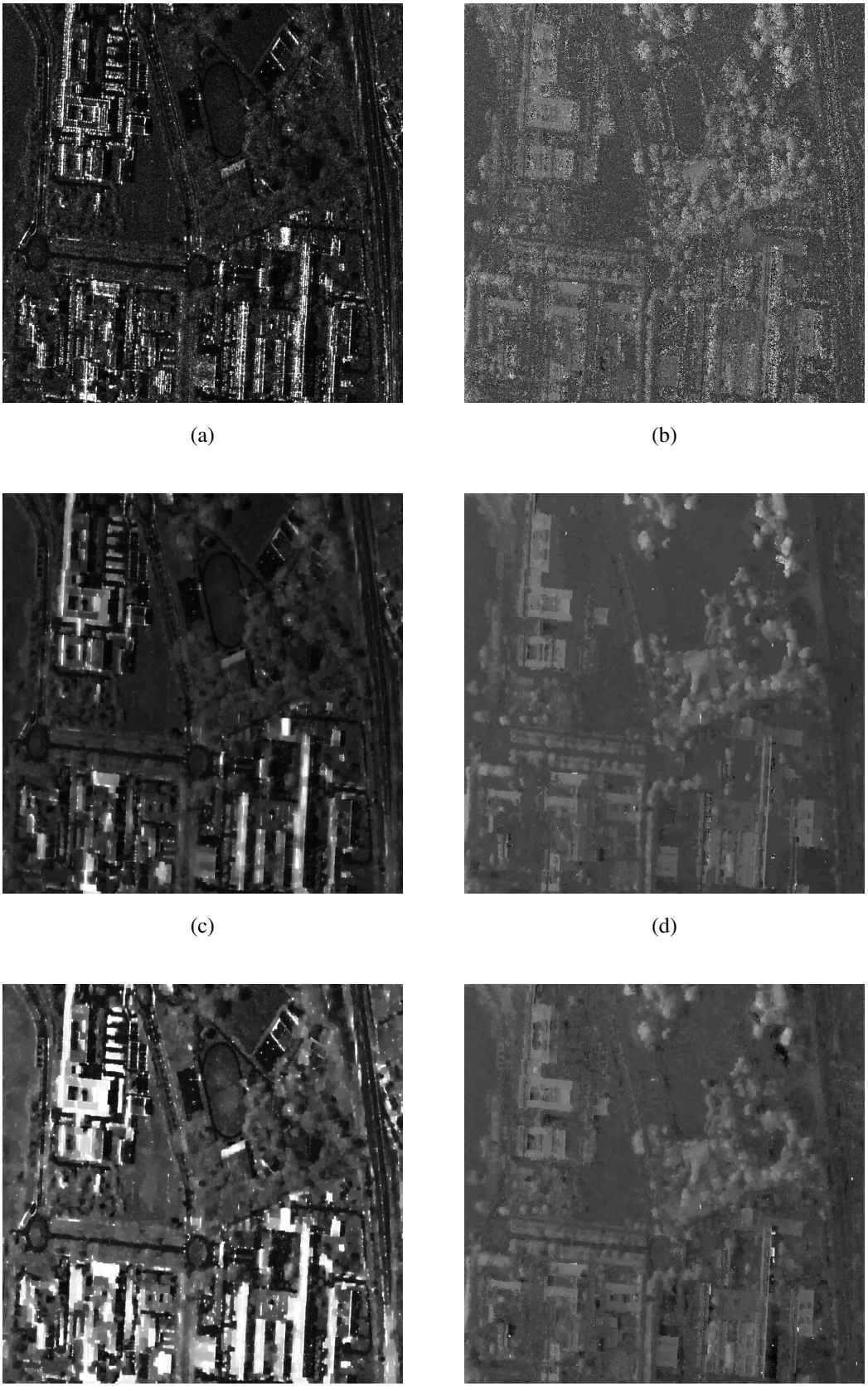

Fig. 5. Original SAR image (a) amplitude and (b) interferometric phase ©DGA/CNES and their joint regularization with the approximate model (c)-(d) and exact joint likelihood model (e)-(f). Images are 1000×1000 pixels and regularization took about 1 minute for the approximate model and 2 minutes and a half for the exact model (two passes of the scaling sampling).

III-C. The input noisy amplitude $\sqrt{\boldsymbol{I}^{(12)}}$ and noisy interferometric phase $\boldsymbol{\varphi}$ are displayed on sub-figures 5(a) and 5(b) respectively. We used the automatic hyper-parameter estimation procedure based on the L-curve corner to set β_a and β_ϕ for each model. The regularized amplitude and phase images for the approximate likelihood model are shown on sub-figures 5(c) and 5(d). On sub-figures 5(e) and 5(f), we show the regularized amplitude and phase obtained with the exact likelihood. Contrary to the results of figure 4 and 5(c)-(d), obtained with the approximate likelihood model, we did not mask the shadow areas to obtain sub-figures 5(e)-(f). The regularized phase is however quite smooth which illustrates the robustness of the exact likelihood model. One can however note that the regularized amplitude is less satisfactory when using this exact model: some values located in low coherence areas are amplified. This can be understood by considering the maximum likelihood amplitude value for a given regularized phase $\boldsymbol{\phi}_s$:

$$\hat{\boldsymbol{a}}_s^{2\,(\mathrm{ML})} = [\boldsymbol{I}_s^{(1)} + \boldsymbol{I}_s^{(2)} - 2 \cdot \boldsymbol{I}_s^{(12)} \cdot \boldsymbol{\zeta}_s \cdot \cos(\boldsymbol{\phi}_s - \boldsymbol{\varphi}_s)]/[2(1 - \boldsymbol{\zeta}_s^2)]. \tag{17}$$

If the regularized phase $\boldsymbol{\phi}_s$ differs from the noisy phase $\boldsymbol{\varphi}_s$, then $\cos(\boldsymbol{\phi}_s - \boldsymbol{\varphi}_s)$ will be much smaller than 1. In a region of low coherence ($\boldsymbol{\zeta}_s$ low), the maximum likelihood value will then be $\hat{\boldsymbol{a}}_s^{2\,(\mathrm{ML})} \gtrapprox (\boldsymbol{I}_s^{(1)} + \boldsymbol{I}_s^{(2)})/[2(1 - \boldsymbol{\zeta}_s^2)]$, corresponding to an amplification of the $2M-$looks amplitude $(\boldsymbol{I}_s^{(1)} + \boldsymbol{I}_s^{(2)})/2$ by a factor at least $1/(1 - \boldsymbol{\zeta}_s^2)$. For 3D reconstruction applications, this not an issue. This would however be a drawback in applications where the exact radiometry is searched.

Moreover, the high non-convexity of the energy to minimize however raises new questions on the closeness of the minimum found to the global minimum. We are confronted to a classical dilemma in MRF models: what is the best compromise achievable between statistical model accuracy and the efficiency of the associated minimization techniques?

IV. Application to 3D reconstruction with InSAR and optical data fusion

We consider in this section how to include in the InSAR regularization process some additional information provided by an optical image. We suppose here that an optical image of the scene acquired with normal incidence is available. The aim is to generalize the previous framework of joint amplitude / interferometric phase regularization to integrate the optical information.

A. Problem statement

The first step is the projection of both data in a common geometry. The projection fuctions depend on the pixel elevation. In this paper, we propose to use the elevation provided by the interferometric phase image to project the pixels in the optical geometry. Unfortunately, after projection, the cloud of points is irregular. Therefore, a triangulation of this cloud is computed. We used QuickHull algorithm to compute a Delaunay triangulation of the points [2]. This triangulation defines a graph, whose nodes are the projected pixels of the SAR image and whose edges are given by the Delaunay triangulation. Since the Markovian framework is applicable for any graph, the whole framework previously described is applicable.

The problem is now stated as follows. Given the observed field $\boldsymbol{u} = [\boldsymbol{e}, \boldsymbol{\varphi}]$ on the graph and the optical data, how to estimate a regularized version $\hat{\boldsymbol{v}}$? We propose to introduce the optical information as an external field $\boldsymbol{o}$. We minimize on the Delaunay graph the following energy:

$$E(\boldsymbol{v}|\boldsymbol{u},\boldsymbol{o}) = \sum_{s} U(\boldsymbol{u}_s|\boldsymbol{v}_s,\boldsymbol{o}) + \beta \sum_{(s,t)} \psi(\boldsymbol{v}_s,\boldsymbol{v}_t|\boldsymbol{o}_s,\boldsymbol{o}_t) \ , \tag{18}$$

If we consider that the likelihood term does not depend on the external field $\boldsymbol{o}$, we can use the same likelihood models as those defined in section III. We design a regularization potential that favors edges in the amplitude and SAR images at the location of the edges of the optical image. The proposed prior model is described in paragraph IV-C.

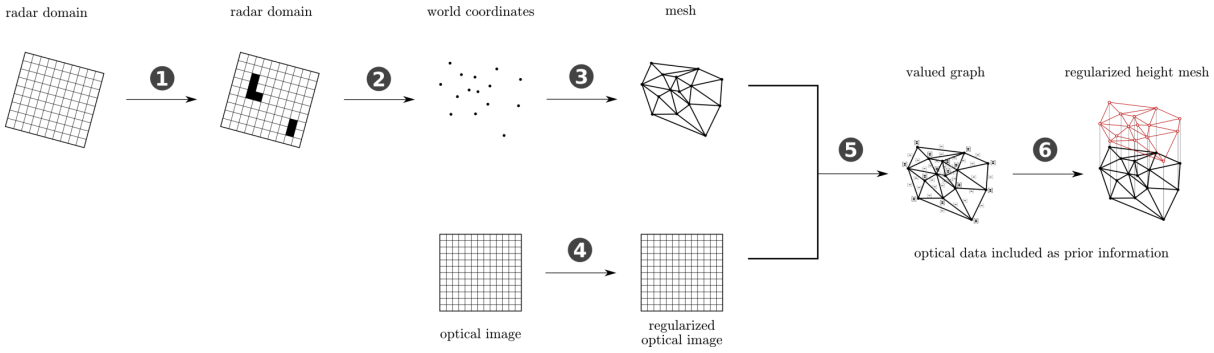

Fig. 6. Scheme of the suggested method. The numbers correspond to the algorithm steps referred to in the text.

The different processing steps of the proposed method are summarized in figure 6. The main steps, denoted with circled numbers on the figure, are the following:

1. The shadows are detected on the radar image.
2. The height map in the world coordinates is obtained by projection of all points from the radar image except those in shadow areas, using the height directly provided by the interferometric phase.
3. The cloud of points of the height map is then triangulated into a mesh by Delaunay triangulation. This mesh defines the topology of the graph used in steps 5 and 6.
4. To ease the introduction of optical information, the optical image is regularized prior to graph construction.
5. A valued graph is then built with nodes corresponding to each of the points of the Delauney graph, arcs given by the mesh and values set using the SAR amplitude, height and the optical information.
6. Once the graph is built, a regularized height mesh is computed by defining a Markov random field over the graph. The optical information is introduced as an external field.

B. Pre-processing steps

Steps 1 to 4 are preprocessing steps required before the actual height regularization (steps 5–6).

1) Pre-processing of the SAR data and projection: As described in the problem statement, before merging the InSAR and optical data to perform a 3D reconstruction, images must be transformed into a common coordinate system. Assuming the optical image is acquired at normal incidence, we then have to project back the InSAR data from distance sampling coordinates to 3D coordinates. Before projecting the points from radar geometry to world coordinates, shadows are detected (step 1) to prevent from projecting points with unknown (i.e., random) height. This detection is made using the Markovian classification described in [38]. Points outside the

shadows are then projected based on their interferometric phase and the radar acquisition parameters (step ❷). This gives a 3D cloud of points (x, y, z) in the world coordinates. The projection of this cloud on a horizontal plane is then triangulated with Delaunay algorithm to obtain a height mesh (step ❸). The height of each node of the obtained graph can then be regularized (see next section).

2) Pre-processing of the optical data: The optical image is simplified using a geometry+texture decomposition [46] before fusion (step ❹). This decomposition is obtained with a TV+L1 regularization computed using the graph cut algorithm described in section II. Figure 7 displays the gradient norm of the optical image before and after its regularization. Most irrelevant edges are removed. Other edge-detection techniques could also be used provided they output edges matching those of the relevant structures.

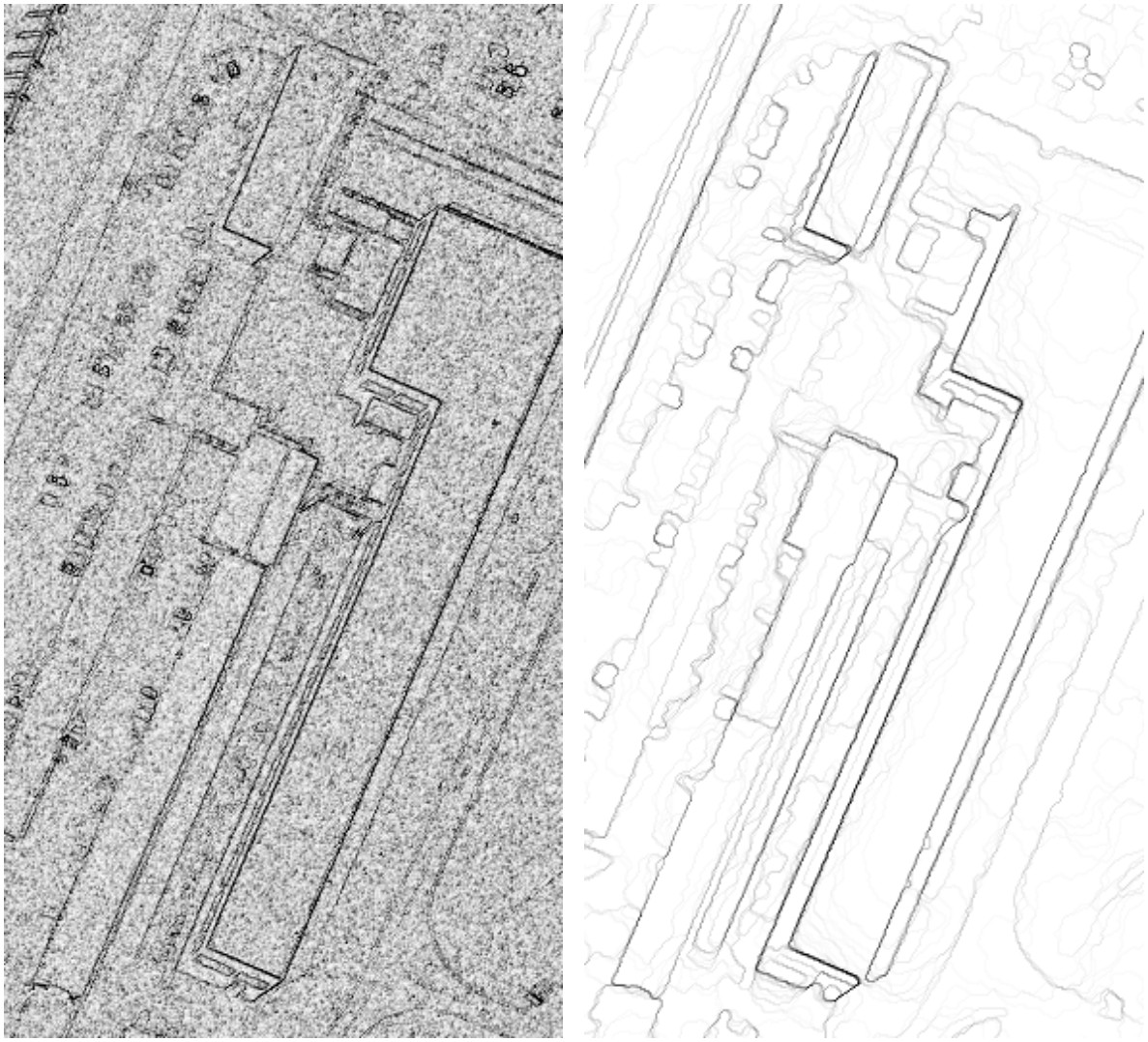

(a) (b)

Fig. 7. Optical image regularization with TV+L1 decomposition model: (a) gradient norm of the optical image before regularization; (b) after regularization, remaining gradients correspond to the building edges.

C. Height regularization model

In this application, the joint information of amplitude and interferometric data is used together with the optical data. Similarly as in the previous section, we define the regularized height field as that which maximizes the posterior probability according to the log-likelihood and log-prior models described below.

1) Log-likelihood model: If we consider the conditional probabilities of amplitude and phase as independent from the external field, we can use one of the two likelihood models described in sections III-B and III-C respectively. We used the separable and approximate model (equations 10 and 11) in the following.

2) Prior model: We propose a prior model that accounts for the phase and amplitude dependency and that introduces the edges of the optical image.

We have chosen here to introduce the optical data as an external field with fixed values. By this way, we introduce the optical image gradient as a prior. Equation 12 is then replaced by:

$$\psi(\boldsymbol{a}_s - \boldsymbol{a}_t, \boldsymbol{\phi}_s - \boldsymbol{\phi}_t | \boldsymbol{o}_s, \boldsymbol{o}_t) = G_{\boldsymbol{o}_s, \boldsymbol{o}_t} \max(|\boldsymbol{a}_s - \boldsymbol{a}_t|, \gamma|\boldsymbol{\phi}_s - \boldsymbol{\phi}_t|) \tag{19}$$

with $G_{\boldsymbol{o}_s, \boldsymbol{o}_t} = \max(0, 1 - k_{opt}|\boldsymbol{o}_s - \boldsymbol{o}_t|)$ an expression that depends on the difference between the values $\boldsymbol{o}_s$ and $\boldsymbol{o}_t$ of the optical image at sites s and t, and k_{opt} a thresholding parameter.

When the optical image is constant between sites s and t, the $G_{\boldsymbol{o}_s, \boldsymbol{o}_t}$ term equals 1 and does not modify the joint TV regularization. When $|\boldsymbol{o}_s - \boldsymbol{o}_t|$ is high (corresponding to a discontinuity), $G_{\boldsymbol{o}_s, \boldsymbol{o}_t}$ is low, thus reducing the regularization of amplitude and phase. This modification helps preserving the building shapes according to the optical data. As the convexity of the regularization potential is preserved, the vectorial algorithm of section II can be used.

Let us note that another alternative to introduce the optical data would have been to jointly regularize the phase, amplitude and optical images by including the optical data in the log-likelihood term and extending equation 19 to include the regularized optical image (i.e., using a ternary $\max$ operator). This latter solution requires to set adequately the weights of each of the terms.

D. Results and discussion

We applied the processing steps summarized in figure 6 to the InSAR and optical images of an industrial area near Dunkerque, France to illustrate the potential of the approach. Figure 8(a) shows the 6 looks interferometric phase used as input. It is far too noisy to be usable directly as an elevation model. We performed a joint amplitude/phase regularization using the optical image as an external field that eases the apparition of edges at the location of the optical image contours. The obtained 3D mesh is displayed on figure 8(b). The surface is smooth with sharp transitions located at the optical image edges. Buildings are clearly above the ground level (note that the shadows of the optical image create a fake 3D impression).

This approach requires a very good registration of the SAR and optical data and implies the knowledge of all acquisition parameters which is not always possible (depending on the source of images). The optical image should be taken with normal incidence to match the radar data. The image displayed on figure 8 was taken with a slight angle that displaces the edges and/or duplicates them. For the method to perform well, the edges of structures must be visible in both optical and InSAR images. The method would benefit from a higher-level edge detection on the optical image (significant edges detection, building detection).

(a) (b)

Fig. 8. Illustration of 3D reconstruction with an additional optical image: (a) interferometric phase; (b) height mesh obtained after joint phase/amplitude regularization with a prior that includes the optical image as an external field. The preprocessed optical image is used as a texture on the 3D mesh.

V. Conclusion

In this paper we have presented two applications of a new optimization algorithm adapted for vectorial data. The first one is dedicated to the joint filtering of phase and amplitude for 3D reconstruction. The second one is the extension of such an approach to introduce information derived from an optical image. The framework described is quite general and can be used to fuse heterogeneous data according to their statistical distribution and to prior knowledge that can be introduced by various ways (edge co-location by joint regularization, variable weights, ...). The discrete minimization algorithm can handle energies with non-convex data-fidelity terms and (possibly non-smooth) convex priors. Such energies arise when modelling speckle noise (non-convex log likelihood) and edge-preserving regularization using total variation. By defining the regularized field over a graph, it is possible to merge images with different sampling/geometry. In both cases promising results are obtained.

Further work will be dedicated to a more extensive testing and evaluation of this framework, specially for the new data that are acquired by TerraSAR-X and CosmoSkyMed. Particularly, the phase filtering should be adjusted to take wrapped phase into account. Concerning the fusion application, one of the main point to be investigated is the accurate registration between optical and SAR sensors with metric resolution data.

The proposed graph-cut based InSAR regularization technique will directly benefit in the near future from the ongoing research on algorithms [5], [24] and fast implementations such as GPU-based approaches [44] that dramatically improve the running time of minimum cut computation.

Acknowledgment

The authors would like to thank CNES, especially C. Tison, for their support, and the Office National d'Études et de Recherches Aérospatiales and the Délégation Générale pour l'Armement for providing the data.

The authors wish to thank the anonymous reviewers for their valuable comments and suggestions, and would like to acknowledge one of the reviewers for suggesting the use of the exact joint likelihood model.

REFERENCES

[1] R. Ahuja, D. Hochbaum, and J. Orlin. Solving the convex cost integer dual network flow problem. *Management Science*, 49(7):950–964, 2003.

[2] C. Bradford Barber, David P. Dobkin, and Hannu Huhdanpaa. The quickhull algorithm for convex hulls. *ACM Trans. Math. Softw.*, 22(4):469–483, 1996.

[3] A. Bendjebbour, Y. Delignon, L. Fouque, V. Samson, and W. Pieczynski. Multisensor images segmentation using Dempster-Shafer fusion in markov fields context. *IEEE Transactions on Geoscience and Remote Sensing*, 39(8):1789–1798, 2001.

[4] J. Besag. On the statistical analysis of dirty pictures. *J. R. Statist. Soc. B*, 48(3):259–302, 1986.

[5] A. Bhusnurmath and C.J. Taylor. Graph Cuts via ℓ_1 Norm Minimization. *IEEE Transactions on Pattern Analysis and Machine Intelligence*, 30(10):1866–1871, 2008.

[6] Y. Boykov and V. Kolmogorov. An experimental comparison of min-cut/max-flow algorithms for energy minimization in vision. *Pattern Analysis and Machine Intelligence, IEEE Transactions on*, 26(9):1124–1137, 2004.

[7] Y. Boykov, O. Veksler, and R. Zabih. Fast approximate energy minimization via graph cuts. *IEEE Transactions on Pattern Analysis and Machine Intelligence*, 26(2):147–159, 2001.

[8] P.L. Combettes and J.C. Pesquet. Image restoration subject to a total variation constraint. *IEEE Transactions on Image Processing*, 13(9):1213–1222, 2004.

[9] J. Darbon. *Composants logiciels et algorithmes de minimisation exacte d'énergies dédiées au traitement des images*. PhD thesis, Ecole Nationale Supérieure des Télécommunications (ENST E050), 2005.

[10] J. Darbon and M. Sigelle. Image restoration with discrete constrained Total Variation part I: Fast and exact optimization. *Journal of Mathematical Imaging and Vision*, 26(3):261–276, December 2006.

[11] J. Darbon and M. Sigelle. Image Restoration with Discrete Constrained Total Variation Part I: Fast and Exact Optimization - Part II: Levelable Functions, Convex Priors and Non-Convex Cases. *Journal of Mathematical Imaging and Vision*, 2006.

[12] J. Darbon and M. Sigelle. Image restoration with discrete constrained Total Variation part II: Levelable functions, convex priors and non-convex cases. *Journal of Mathematical Imaging and Vision*, 26(3):277–291, December 2006.

[13] L. Denis, F. Tupin, J. Darbon, and M. Sigelle. SAR image regularization with fast approximate discrete minimization. CAM Report 07-38 (available at ftp://ftp.math.ucla.edu/pub/camreport/cam07-38.pdf), UCLA, 2007.

[14] L. Denis, F. Tupin, J. Darbon, and M. Sigelle. Joint filtering of SAR interferometric phase and amplitude data in urban areas by TV minimization. In *IGARSS'08*, Boston, USA, jul 2008.

[15] S. Geman and D. Geman. Stochastic Relaxation, Gibbs Distribution, and the Bayesian Restoration of Images. *IEEE Transactions on Pattern Analysis and Machine Intelligence*, PAMI-6(6):721–741, November 1984.

[16] J.W Goodman. Statistical properties of laser speckle patterns. In *Laser Speckle and Related Phenomena*, volume 9, pages 9–75. J.C Dainty (Springer Verlag, Heidelberg, 1975), 1975.

[17] P.C. Hansen and D.P. O'Leary. The Use of the L-Curve in the Regularization of Discrete Ill-Posed Problems. *SIAM Journal on Scientific Computing*, 14:1487, 1993.

[18] H. Ishikawa. Exact optimization for Markov random fields with convex priors. *IEEE Trans. on Pattern Analysis and Machine Intelligence*, 25(10):1333–1336, October 2003.

[19] J.Bioucas-Dias, V. Katkovnik, J. Astola, and K. Egiazarian. Absolute phase estimation: adaptive local denoising and global unwrapping. *Applied Optics*, 47(29):5358–5369, 2008.

[20] J.Dias and J. Leitao. The $\mathbb{Z}\pi M$ algorithm for interferometric image reconstruction in SAR/SAS. *IEEE Transactions on Image processing*, 11(4), 2002.

[21] M. Jäger, A. Reigber, and O. Hellwich. Unsupervised classification of polarimetric SAR data using graph-cut optimization. *IGARSS'07*, 2007.

[22] V. Kolmogorov and A. Shioura. New Algorithms for the Dual of the Convex Cost Network Flow Problem with Application to Computer Vision. *Technical report, http://www.adastral.ucl.ac.uk/~vladkolm/papers/CONVEX_MRF.html*, 2007.

[23] V. Kolmogorov and R. Zabih. What energy functions can be minimized via graph-cuts ? *IEEE Trans. on Pattern Analysis and Machine Intelligence*, 26(2), 2004.

[24] N. Komodakis, G. Tziritas, and N. Paragios. Performance vs computational efficiency for optimizing single and dynamic MRFs: Setting the state of the art with primal-dual strategies. *Computer Vision and Image Understanding*, 112(1):14–29, 2008.

[25] J. S. Lee and I. Jurkevich. Speckle filtering of synthetic aperture radar images : A review. *Remote Sensing Reviews*, 8:313–340, 1994.

[26] F. Lombardini, F. Bordoni, and F. Gini. Feasibility study of along-track SAR interferometry with the COSMO-Skymed satellite system. In *IGARSS04*, volume 5, pages 337–3340, 2004.

[27] H. Maitre. *Processing of Synthetic Aperture Radar Images*. Wiley-ISTE, 2008.

[28] Y. Meyer. *Oscillating Patterns in Image Processing and Nonlinear Evolution Equations*. American Mathematical Society, 2001.

[29] F. Perez Nava, A. Perez Nava, J. Galvez Lamolda, and M. Fuentes Redondo. Change detection for remote sensing images with graph cuts. *SPIE, Image and Signal Processing for Remote Sensing XI*, 5982:229–242, 2005.

[30] M. Nikolova. A variational approach to remove outliers and impulse no ise. *Journal of Mathematical Imaging and Vision*, 20:99–120, 2004.

[31] S. Osher, M. Burger, D. Goldfarb, J. Xu, and W. Yin. An Iterative Regularization Method for Total Variation Based Image Restoration. *SIAM journal on Multiscale modeling and Application*, 4:460–489, 2005.

[32] V. Pascazio and G. Shirinzi. Multifrequency InSAR height reconstruction using through maximum likelihood estimation of local planes parameters. *IEEE Trans. on Image Processing*, 11(12):1478–1489, 2002.

[33] R. Romeiser and H. Runge. Theoretical evaluation of several possible along-track InSAR modes of TerraSAR-X for ocean current measurements. *IEEE Transactions on Geoscience and Remote Sensing*, 45:21–35, 2007.

[34] L. Rudin, S. Osher, and E. Fatemi. Nonlinear total variation based noise removal algorithms. *Physica D.*, 60:259–268, 1992.

[35] S. Serpico and G. Moser. Weight Parameter Optimization by the Kashyap Algorithm in MRF Models for Supervised Image Classification. *IEEE Transactions on Geoscience and Remote Sensing*, 44(12):3695–3705, 2006.

[36] P. C. Smits and S. G. Dellepiane. Synthetic aperture radar image segmentation detail preserving markov random field approach. *IEEE Transactions on Geoscience and Remote Sensing*, 35(4):844–857, 1997.

[37] C. Tison, J.M. Nicolas, F. Tupin, and H. Maître. A New Statistical Model of Urban Areas in High Resolution sar Images for Markovian Segmentation. *IEEE Transactions on Geoscience and Remote Sensing (IGARSS'03 special issue)*, 42(10):2046–2057, oct 2004.

[38] C. Tison, J.M. Nicolas, F. Tupin, and H. Maître. A New Statistical Model of Urban Areas in High Resolution sar Images for Markovian Segmentation. *IEEE Transactions on Geoscience and Remote Sensing (IGARSS'03 special issue)*, 42(10):2046–2057, oct 2004.

[39] C. Tison, F. Tupin, and H. Maître. A fusion scheme for joint retrieval of urban map and classification from high resolution interferometric SAR images. *IEEE Transactions on Geoscience and remote Sensing*, 45(2):495–505, mar 2007.

[40] R. Touzi. A review of speckle filtering in the context of estimation theory. *IEEE Transactions on Geoscience and Remote Sensing*, 40(11):2392–2404, 2002.

[41] R. Touzi and A. Lopes. Statistics of the Stokes parameters and of the complex coherenceparameters in one-look and multilook speckle fields. *IEEE Transactions on Geoscience and Remote Sensing*, 34(2):519–531, 1996.

[42] E. Trouvé, M. Caramma, and H. Maître. Fringe detection in noisy complex interferograms. *Applied Optics*, 35(20):3799–3806, July 1996.

[43] F. Tupin and M. Roux. Markov Random Field on Region Adjacency Graphs for the fusion of SAR and optical data in radargrammetric applications. *IEEE Transactions on Geoscience and Remote Sensing*, 43(8):1920–1928, aug 2005.

[44] V. Vineet and PJ Narayanan. CUDA cuts: Fast graph cuts on the GPU. In *IEEE Computer Society Conference on Computer Vision and Pattern Recognition Workshops, 2008. CVPR Workshops 2008*, pages 1–8, 2008.

[45] M. Walessa and M. Datcu. Model-based despeckling and information extraction of SAR images. *IEEE Transactions on Geoscience and Remote Sensing*, 38(5), 2000.

[46] W. Yin, D. Goldfarb, and S. Osher. A comparison of three total variation based texture extraction models. *Journal of Visual Communication and Image Representation*, 18(3):240–252, 2007.

[47] B. Zalesky. Efficient Determination of Gibbs Estimators with Submodular Energy Functions. *arXiv:math/0304041v1[math.OC]*, 2003.